

Journal of Biomedical Optics

SPIEDigitalLibrary.org/jbo

Degradation in the degree of polarization in human retinal nerve fiber layer

Biwei Yin
Bingqing Wang
Henry G. Rylander, III
Thomas E. Milner

Degradation in the degree of polarization in human retinal nerve fiber layer

Biwei Yin,^{a,*} Bingqing Wang,^b Henry G. Rylander III,^b and Thomas E. Milner^b

^aUniversity of Texas at Austin, Departments of Electrical and Computer Engineering, 1 University Station C0803, Austin, Texas 78712

^bUniversity of Texas at Austin, Department of Biomedical Engineering, 1 University Station, C0800, Austin, Texas 78712

Abstract. Using a fiber-based swept-source (SS) polarization-sensitive optical coherence tomography (PS-OCT) system, we investigate the degree of polarization (DOP) of light backscattered from the retinal nerve fiber layer (RNFL) in normal human subjects. Algorithms for processing data were developed to analyze the deviation in phase retardation and intensity of backscattered light in directions parallel and perpendicular to the nerve fiber axis (fast and slow axes of RNFL). Considering superior, inferior, and nasal quadrants, we observe the strongest degradation in the DOP with increasing RNFL depth in the temporal quadrant. Retinal ganglion cell axons in normal human subjects are known to have the smallest diameter in the temporal quadrant, and the greater degradation observed in the DOP suggests that higher polarimetric noise may be associated with neural structure in the temporal RNFL. The association between depth degradation in the DOP and RNFL structural properties may broaden the utility of PS-OCT as a functional imaging technique.

© The Authors. Published by SPIE under a Creative Commons Attribution 3.0 Unported License. Distribution or reproduction of this work in whole or in part requires full attribution of the original publication, including its DOI. [DOI: [10.1117/1.JBO.19.1.016001](https://doi.org/10.1117/1.JBO.19.1.016001)]

Keywords: optical coherence tomography; polarization-sensitive; imaging; retinal nerve fiber layer; degree of polarization; degree of coherence.

Paper 130543RRR received Jul. 31, 2013; revised manuscript received Dec. 2, 2013; accepted for publication Dec. 4, 2013; published online Jan. 3, 2014.

1 Introduction

Optical coherence tomography (OCT) is a noninvasive cross-sectional imaging technique first introduced in 1991 as a time-domain (TD) technique¹ and later as a Fourier-domain (FD) approach in 1995.^{2,3} To date, two FD-OCT instrumentation approaches have been utilized, including spectrometer-based OCT and swept-source (SS)-OCT.²⁻⁵ The FD-OCT has higher sensitivity and acquisition speed than TD-OCT,⁵⁻⁷ and recently, SS-OCT with A-scan rate up to 5 MHz has been demonstrated using an FD mode-locked (FDML) laser.⁸

Polarization-sensitive (PS)-OCT is a functional extension of OCT. In addition to intensity imaging, PS-OCT can provide a measure of a biological sample's birefringence properties (i.e., birefringence, phase retardation, and optical axis orientation). The PS-OCT was first implemented in a bulk optics system,^{9,10} since polarization state of light can be easily controlled and preserved in free space. Later, fiber-based PS-OCT systems were developed and demonstrated.¹¹⁻¹³ Compared with PS-OCT systems using bulk optics, fiber-based systems provide convenience in alignment but at the cost of polarization-mode dispersion (PMD), additional processing of detected polarization data, and more complex hardware. Both polarization-maintaining fiber (PMF) and standard single-mode fiber (SMF) have been implemented for PS-OCT system construction.¹⁴⁻²⁷ The PMF-based PS-OCT systems take advantage of PMF's property that light propagation in two orthogonal linear polarization states can be maintained. Due to different propagation velocities of the light in two orthogonal states, however, length mismatch of sample and reference paths is normally compensated by hardware or software.¹⁴⁻¹⁶ Due to the fact that SMF introduces

a unitary transformation and transforms the polarization state of transmitted light, the polarization signal acquired by a PS-OCT system utilizing SMF has to be reinterpreted, and different methodologies have been proposed.¹⁷⁻²⁴

The PS-OCT has been applied in ophthalmology to investigate birefringence of ocular structures including the cornea, crystalline lens, and the retinal nerve fiber layer (RNFL). Since RNFL is known to be birefringent with microtubules within retinal ganglion cells (RGCs) contributing significantly to the form birefringence,²⁸ measurement of RNFL birefringence can be used to monitor structural changes in the cytoskeleton of RGCs associated with retinal neuropathies such as glaucoma.

This study investigates the degradation in the degree of polarization (DOP) of light backscattered from human RNFL with increasing depth. The DOP is usually defined as the ratio of intensity of completely polarized light to the total intensity of light. The DOP is unity for purely polarized light, smaller than unity for partially polarized light, and zero for unpolarized light. Recently the DOP uniformity (DOPU)²⁹ was introduced by Göttinger et al. to examine the depth-resolved uniformity of backscattered light's polarization state represented by Stokes parameters on the Poincaré sphere for multiple A-scans within a small sample region. The processing method we employed for this study is also based on analyzing multiple A-scans within a small sample region; we use a Jones vector representation in the native sample frame (SF) of the RNFL so that the amplitude and phase of backscattered light can be utilized for statistical analysis to investigate the DOP degradation in RNFL.

Factors that may contribute to the degradation of DOP with increasing depth in biological tissue include multiple forward scattering events in which light travels through different paths but is singly backscattered, polarization state changes when light is forward or backward scattered by irregularly shaped particles,

*Address all correspondence to: Biwei Yin, E-mail: biwei.yin@gmail.com

and speckle noise and signal-to-noise (SNR) degradation with increasing depth.³⁰ An SMF-based SS PS-OCT clinical system was constructed and utilized to measure the reduction of the DOP with depth in human RNFL and the differences in degradation in DOP in superior, temporal, inferior, and nasal quadrants.

2 Methodology

2.1 Clinical PS-OCT System

The clinical PS-OCT (Fig. 1) system utilized a SS laser (HSL-1000 by Santec Corp., Komaki, Aichi, Japan) with a sweep rate of 28 kHz, 1064-nm center wavelength, and a spectral scan range of 80 nm, providing an axial resolution of 12 μm in tissue, which is poorer than expected due to dispersion and deviations from a Gaussian-shaped laser power spectral density profile. A polarization controller consisting of a linear polarizer and a phase modulator is utilized to provide three incident polarization states into the interferometer. The phase modulator is composed of two lithium niobate (LiNbO_3) crystals with fast and slow axes oriented at 45 deg to the linear polarizer. The two LiNbO_3 crystals are of equal length and the fast axis of one is coaligned with the slow axis of the other to balance intrinsic birefringence and remove PMD. A high-voltage amplifier controls the phase retardation in the two crystals. The voltage applied to the phase modulator is adjusted to provide three polarization states with Stokes vectors (Q, U, V) in the right-handed laboratory frame (LF) being $(1, 0, 0)$, $(-\sin 30 \text{ deg}, 0, \sin 60 \text{ deg})$, and $(-\sin 30 \text{ deg}, 0, -\sin 60 \text{ deg})$.²² In the LF, the horizontal axis is along x , vertical (along gravity) is along y , and the light propagates along the z -direction. A 30/70 fiber coupler splits source light into sample and reference arms. In the sample

arm, an interface simultaneously delivers OCT light (0.86 mW average power) together with a line-scanning laser ophthalmoscope light onto the patient's cornea. Light in the reference arm has two paths: one is connected to a balanced detection module to interfere with sample light and the other splits into system trigger and an electronic circuit for a resampling clock. A Mach-Zehnder interferometer is used to generate a resampling clock signal and is connected to an external circuit board to quadruple the clock frequency. Light reflected from the sample interferes with reference light in a bulk optics-balanced detection module. Reference light goes through a polarizer oriented at 45 deg to the vertical (y) axis before interfering to ensure equal intensity and zero-phase delay in horizontal and vertical polarization states. A nonpolarizing crystal beam splitter is used for balanced detection, and two polarization beam splitters separate interference signals into vertical and horizontal channels. The bulk optics-balanced detection module used for polarization detection eliminates unbalanced polarization transformations between the two detection arms.

A cluster ring scan pattern is utilized for patient imaging: 10 rings are concentric about the optic nerve head with diameters ranging from 2 to 5 mm; each ring contains 36 clusters corresponding to a 10-deg angular separation, and each cluster consists of 100 A-scans acquired over a small spatial region. Since the 100 A-scans in each cluster are taken as uncorrelated and share nearly equivalent sample structural features, average of 100 A-scans' intensity data gives an intensity image with reduced speckle noise and is utilized for RNFL segmentation of the cluster. Detection of the anterior and posterior RNFL boundaries is based on an automatic intensity threshold approach and, when necessary, manually corrected by visual inspection.

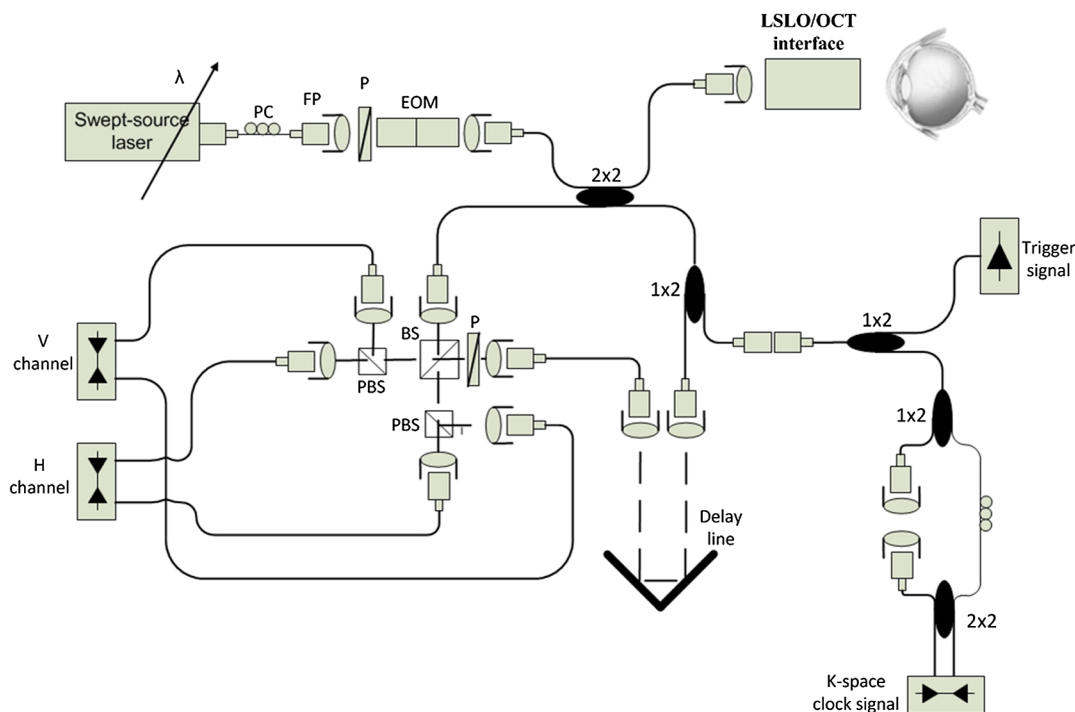


Fig. 1 Clinical swept-source (SS) polarization-sensitive (PS) optical coherence tomography (OCT) system. PC: polarization controller; FP: fiber port; P: polarizer; EOM: broadband electro-optic modulator; BS: nonpolarization beam splitter; PBS: polarization beam splitter.

2.2 Polarization Processing

Jones matrix and Stokes vector formalisms were applied for polarization data processing. Briefly, in the absence of diattenuation,³¹ when light propagates through a uniform birefringent layer, the trajectory of normalized Stokes vectors of backscattered light rotates about an eigen-axis on the Poincaré sphere. Effect of polarization transformations in the SMF causes a rotation of the eigen-axis away from the equator of the Poincaré sphere.^{17,31,32} If the SMF remains stable while switching between incident polarization states, equivalent transformations of three incident polarization states are produced giving three arcs on the Poincaré sphere with a common rotation axis. Starting from two orthogonal channels' signal amplitude and phase difference (Box 1 in Fig. 2) for each incident state, depth-resolved normalized Stokes vectors for 100 A-scans are constructed (Box 2.1 in Fig. 2) and then are averaged and normalized to reduce polarimetric noise by a factor of approximately 10 (Box 3 in Fig. 2); ideally these three arcs rotate about a common axis corresponding to RNFL's optical axis. The trajectories on the Poincaré sphere corresponding to the three incident states are constructed based on averaged and

normalized Stokes vectors. The Stokes vector of the optical axis is determined by using a Levenberg–Marquardt nonlinear least-squares fitting algorithm to find a single vector originating from the center of Poincaré sphere to be the rotation axis of all three arcs (Box 4 in Fig. 2). Note that whether this vector represents the fast or slow axis can be determined by the direction of rotation of the trajectory with increasing RNFL depth. Fast and slow axes are orthogonal to each other in the Jones vector formalism; on the Poincaré sphere, their Stokes vector representations are on polar-opposite sides.

In the Jones vector calculus, (E_x, E_y) represents a polarization state, where the two components E_x and E_y represent analytic signals for the complex electric field along the x - and the y -axis in the LF. Depth-resolved Jones vector for each A-scan in LF can be constructed based on the detected signal (Box 2.2 in Fig. 2). In a linearly form-birefringent fibrous tissue, fast and slow axes correspond to directions parallel and perpendicular to the tissue fiber orientation.³³ We adopt a Jones vector formulation by assuming a coordinate system parallel and perpendicular to the fiber orientation to analyze propagation of amplitude and phase of backscattered light in the native coordinate system of the fibrous tissue SF.

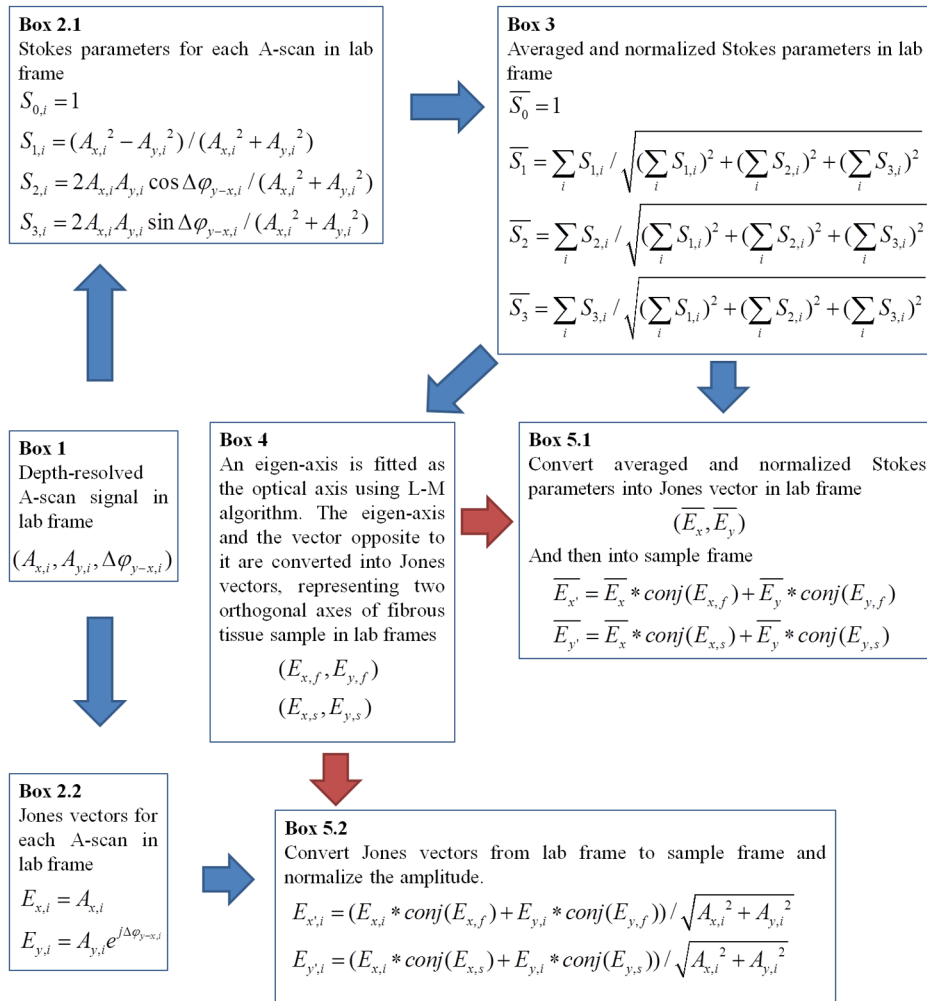


Fig. 2 Flow chart diagram of processing to transform depth-resolved polarization data from the laboratory frame (LF) into the fibrous tissue sample frame (SF). Blue arrows indicate the data transformation, red arrows indicate that the fast and slow axes determined in Box 4 are applied in Boxes 5.1 and 5.2 for conversion from LF to SF, and *conj* refers to complex conjugate.

Depth-resolved polarization data are transformed from the LF into SF by projecting their Jones vectors onto fast and slow axes of the fibrous tissue sample (Boxes 5.1 and 5.2 in Fig. 2). In Fig. 2, subscripts x and y represent two orthogonal axes in the LF; subscripts x' and y' represent two orthogonal axes in the SF; subscripts f and s represent fast and slow axes of the fibrous tissue sample; and subscript i refers to a single A-scan.

After obtaining depth-resolved Jones vectors of backscattered light in the SF, the phase difference $\Delta\varphi_{y'-x'}$ between $\vec{E}_{x'}$ and $\vec{E}_{y'}$ is the phase retardation introduced by the sample birefringence. Since the RNFL is assumed to be a linearly birefringent layer, a linear fit is applied to phase retardation data $\Delta\varphi_{y'-x'}$ with respect to sample depth; phase retardation values on the fitted lines are taken as the best estimate of phase retardation ($\Delta\varphi_{y'-x',i}$) at that depth, whereas the slope of this linear fit indicates phase retardation per unit RNFL thickness or RNFL birefringence. Each cluster is interrogated by three incident polarization states. Under ideal conditions, three states' phase retardation per unit depth should be identical, and as a linear fit is applied separately for each incident state, phase retardation per unit depth for different incident states may vary from each other slightly, which can be caused by measurement error and polarimetric noise.

To investigate degradation in DOP with increasing RNFL depth, each cluster's 100 A-scans is also converted from the LF to the SF ($E_{x',i}, E_{y',i}$) based on the same optical axes, and the phase retardation $\Delta\varphi_{y'-x',i}$ is computed versus depth for each A-scan.

In polarization optics, the coherency matrix J is defined as³⁴

$$J = \begin{bmatrix} J_{xx} & J_{xy} \\ J_{yx} & J_{yy} \end{bmatrix} = \begin{bmatrix} \langle E_x E_x^* \rangle & \langle E_x E_y^* \rangle \\ \langle E_y E_x^* \rangle & \langle E_y E_y^* \rangle \end{bmatrix}, \quad (1)$$

where E_x and E_y are the complex electric fields along two orthogonal axes, the bracket represents time average, and the “*” refers to complex conjugate. J_{xx} and J_{yy} are the intensity of the electrical field along the two axes, J_{xy} and J_{yx} are the complex conjugates to each other, and the phase is the effective phase $[\arg(J_{xy})]$ retardation between the two axes. The DOP, P , is written as in Eq. (2)³⁴

$$P = \sqrt{1 - \frac{4|J|}{(J_{xx} + J_{yy})^2}} = \sqrt{1 - \frac{4(J_{xx}J_{yy} - J_{xy}J_{yx})}{(J_{xx} + J_{yy})^2}}. \quad (2)$$

According to Eqs. (1) and (2), a more randomized phase difference between E_x and E_y corresponds to an average value of $E_x E_y^*$ or $E_y E_x^*$ (J_{xy} or J_{yx}) closer to zero, resulting in a smaller DOP. Moreover, normalized J_{xy} is written as j_{xy} in Eq. (3), and the absolute value, $|j_{xy}|$, represents the degree of coherence between light oscillations along the two axes. Unlike DOP, the degree of coherence depends on the coordinate system, and it shows the correlation between electric fields along two orthogonal axes. Randomization of phase difference between the two axes corresponds to a reduced degree of coherence.

$$j_{xy} = \frac{J_{xy}}{\sqrt{J_{xx}}\sqrt{J_{yy}}}. \quad (3)$$

We investigate depth-resolved changes in the DOP and degree of coherence of backscattered light in the SF corresponding to directions parallel and perpendicular to the nerve fibers. The deviation of phase retardations [$\text{std}(\Delta\phi)$] of 100 A-scans

from fitted values $\Delta\varphi_{y'-x',t}$ is calculated at each depth position [Eq. (4)]. The statistics we analyze for one cluster's polarization data correspond to slightly offset spatial positions recorded at different times. To account for the phase variation introduced by SNR degradation, a weighting factor (w_i) is applied in Eq. (4). As phase variation introduced by signal degradation is proportional to $1/\text{SNR}$,^{35,36} the ratio of pixel signal strength (S_i) to maximum signal (S_{\max}) in the image is used as the weighting factor w_i (here, we make the assumption that thermal, shot, and intensity noise contributions are white and thus independent of depth).

$$\text{std}(\Delta\phi) = \sqrt{\left[\sum_{i=1}^{i=N} w_i (\Delta\varphi_{y'-x',i} - \Delta\varphi_{y'-x',t})^2 \right] / N} \quad (4)$$

$$w_i = S_i / S_{\max}.$$

Larger values of $\text{std}(\Delta\phi)$ correspond to a lower DOP in the RNFL, and increased deviation with increasing RNFL depth indicate degradation in DOP associated with a depolarization process when light propagates through the RNFL. In addition, standard deviation of the normalized amplitude of the 100 A-scans parallel and perpendicular to fiber axes is also calculated [Eq. (5)].

$$\text{std}(|E_{x'}|) = \sqrt{\left[\sum_{i=1}^{i=N} (|E_{x',i}| - |E_{x',i}^-|)^2 \right] / N}$$

$$\text{std}(|E_{y'}|) = \sqrt{\left[\sum_{i=1}^{i=N} (|E_{y',i}| - |E_{y',i}^-|)^2 \right] / N}. \quad (5)$$

3 Results

3.1 RNFL Intensity Image and Segmentation

An RNFL cluster ring scan (4-mm diameter) intensity image of a 28-year-old healthy female subject's left eye (Fig. 3) centered on the optic nerve head is recorded. Ring scans start in the superior quadrant, and pass through temporal, inferior, and nasal quadrants. A total of 36 clusters (cluster 0 to cluster 35) is divided into four quadrants: superior quadrant (clusters 0 to 5 and clusters 30 to 35 spanning an azimuthal angle of 120 deg), temporal quadrant (clusters 6 to 10 spanning an azimuthal angle of 50 deg), inferior quadrant (clusters 11 to 22 spanning an azimuthal angle of 120 deg), and the nasal quadrant (clusters 23 to 29 spanning an azimuthal angle of 70 deg). In the measurement, clusters that correspond to each quadrant may vary or shift by two or three clusters due to patient movement or subject differences. As shown in Fig. 3, each cluster consists of 100 A-scans, the average of 100 A-scans' intensity signal is used for cluster segmentation, and anterior and posterior RNFL boundaries are found based on intensity thresholding and, when necessary, manually corrected by visual inspection.

3.2 Birefringence and Deviation of Phase Retardation and Intensity

The PS-OCT signal processing method described above (Sec. 2.2 and Fig. 2) uses a Levenberg–Marquardt fitting algorithm on the Poincaré sphere. To examine changes in the DOP

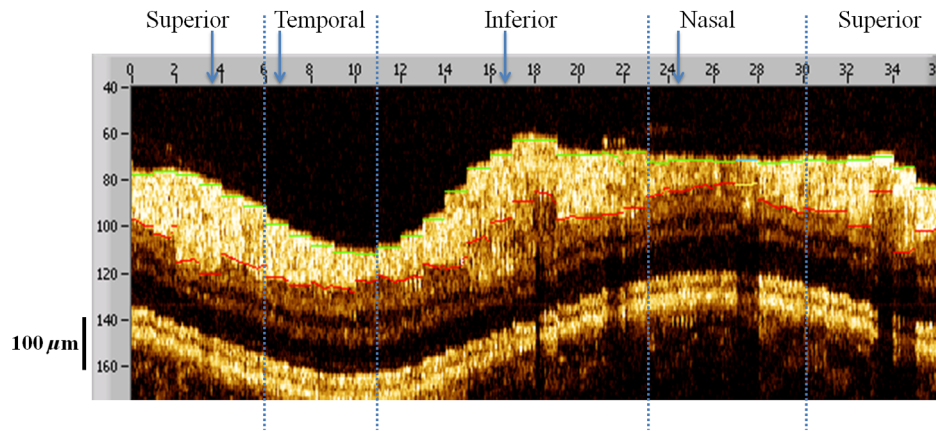


Fig. 3 A cluster ring scan intensity image of RNFL of a 28-year-old healthy female subject's left eye. Vertical axis represents pixel in depth; horizontal axis on top represents cluster number (0 to 35); green and red bars indicate anterior and posterior RNFL boundaries, respectively; and blue dashed lines indicate boundaries of quadrants. Arrows indicate clusters 3, 6, 16, and 24.

when light propagates in RNFL, we present four clusters' phase retardation of three incident states, phase retardation deviation, and standard deviation of intensity parallel and perpendicular to the RNFL fiber axis, each with 100 A-scans (Fig. 4). For comparison, four clusters (3, 6, 16, and 24) are indicated in the intensity image (Fig. 3) with each representing a typical cluster in superior (3), temporal (6), inferior (16), and nasal (24) quadrants.

Phase retardation between fast and slow axes versus RNFL depth (Fig. 4) is calculated based on averaged PS-OCT data of 100 A-scans and increased with depth, because the RNFL is a weakly birefringent layer. A linear fit is applied to estimate the birefringence (phase retardation per unit depth) for each incident polarization state. Three incident polarization states are separated with different incident polarization states introduced by the LiNbO₃ polarization modulator. Slope of the linear fit is phase retardation per unit depth; average of the slope over the three states gives cluster birefringence. The cluster in the superior quadrant has a birefringence of 4.44×10^{-4} , cluster in the temporal quadrant has a birefringence of 2.31×10^{-4} , cluster in the inferior quadrant has a birefringence of 3.69×10^{-4} , and cluster in the nasal quadrant has a birefringence of 1.99×10^{-4} . These birefringence values are consistent with values for human RNFL reported previously.^{24,37-39} Phase retardation deviation is computed by comparing values from each A-scan with the fitted value [Eq. (4)]. The deviation is considered to be introduced by polarimetric noise. As shown in the second column of Fig. 4, though the deviation oscillates about the linear trend line, a general increasing trend in the deviation is observed with increasing RNFL depth, suggesting degradation in the DOP with increasing depth due to varying phases.

Differing from clusters in superior, inferior, and nasal quadrants, the increase in phase retardation deviation at the last two pixels of the temporal cluster (second row in Fig. 4) exhibits much higher values, suggesting a more significant depolarization process. As we rule out the possibility that this abrupt change in phase retardation deviation may be an artifact due to boundary misdetection [the anterior and posterior RNFL boundaries of the clusters presented in Fig. 4 are segmented correctly and conservatively as labeled in the ring scan intensity image (Fig. 3)] and the neighboring clusters exhibit similar features, we hypothesize that the posterior RNFL in the temporal

quadrant scrambles the phase of polarized light more significantly than other quadrants. To quantitatively estimate the increasing trend of deviation, we use a linear fit to characterize the deviation: a larger fitted slope to the trend indicates a more rapid depolarization and faster reduction in the DOP with increasing RNFL depth. Because a model to characterize the depolarization effect with respect to RNFL depth is not developed, a linear fit has the advantage to constrain the fitting curve to most of the data without being disturbed by abrupt changes and clearly illustrates the data trend. Effects not related to optical activity in RNFL (such as abrupt deviation increase due to boundary misdetection) can be minimized. Deviations in the light amplitudes parallel and perpendicular to nerve fiber are also computed. Amplitude deviations along the fast and slow axes follow each other closely and increase with depth similar to phase retardation deviation. The results suggest that degradation in the DOP with increasing RNFL depth is associated with both randomization of phase retardation and an energy transfer between light oscillations parallel and perpendicular to the nerve fiber axes.

3.3 Differences in Degradation in DOP Between Quadrants

The increased deviation in phase retardation and amplitude with RNFL depth is clearly observed (Fig. 4). Phase retardation deviation slope (PRDS) and amplitude deviation slope (ADS) of all 36 clusters are computed and presented in Fig. 5. For comparison, quadrants are separated by dashed lines in Fig. 5 based on the azimuthal angular boundaries indicated above. Clusters in superior and inferior quadrants have relatively small PRDS and ADS, clusters in the nasal quadrant exhibit larger PRDS and ADS, and clusters in the temporal quadrant have the highest PRDS and ADS, which corresponds to the most rapid degradation in the DOP with increased RNFL depth.

3.4 Clinical Study

The PS-OCT retinal data from 10 healthy subjects with ages ranging from 20 to 70 years were collected for this study. All clinical data were collected with IRB approval, and the

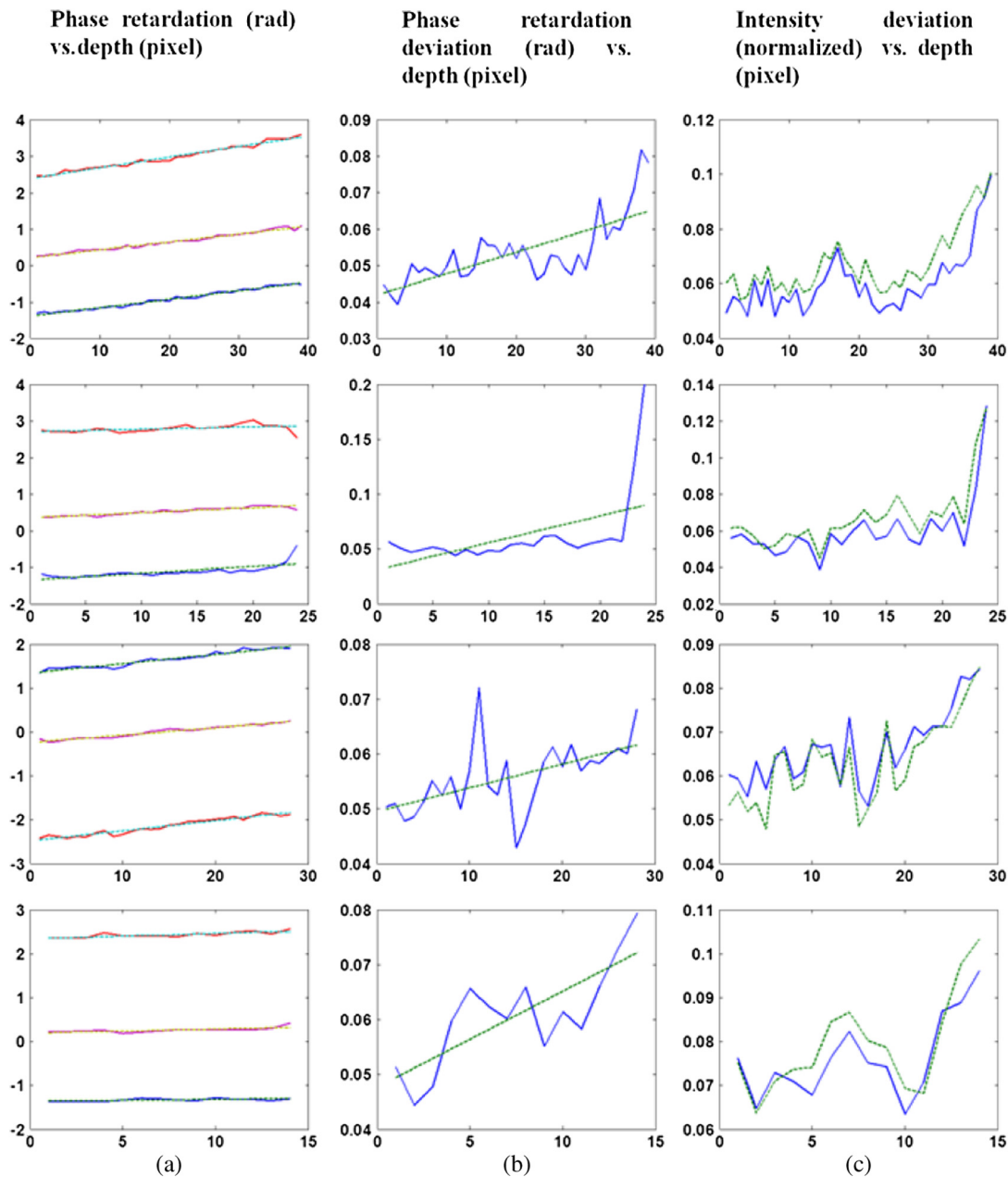


Fig. 4 Cluster phase retardation versus RNFL depth [column (a)], phase retardation deviation versus RNFL depth [column (b)], and intensity deviation of amplitudes parallel and perpendicular to fiber axes versus RNFL depth [column (c)]. Each row represents one cluster: top row is in the superior quadrant, second row from the top is in temporal quadrant, third row from the top is in the inferior quadrant, and bottom row is in the nasal quadrant. Column (a) shows phase retardation between fast and slow axes with respect to RNFL depth: vertical axis represents phase retardation in radians, horizontal axis is RNFL depth in pixels, three solid curves correspond to three incident polarization states on the retina, and the dashed lines are a linear fit. Column (b) is phase retardation deviation (rad) with respect to depth (pixel), solid curve is the total deviation of three incident states, and dashed line is a linear fit to estimate the increasing trend of the phase retardation deviation with depth. Column (c) is intensity deviation with RNFL depth, solid curve is the intensity deviation of normalized field amplitude along the fast axis, and dashed curve is the intensity deviation of the normalized field amplitude along the slow axis, intensity deviation is the total deviation of three incident states. Each pixel corresponds to a $4.7\text{-}\mu\text{m}$ physical length in the RNFL.

clinical trial is registered as NCT01222065. Cluster polarization data were recorded at rings with diameters 3 to 4 mm centered on the optic nerve head (right eye in four subjects and left eye in six subjects) and processed to obtain the PRDS and ADS of each cluster. For each subject, the average of PRDS is calculated for each quadrant (R_1 , R_2 , R_3 , and R_4) to represent the reduction of DOP in the quadrant (subscripts 1 to 4 correspond to

superior, temporal, inferior, and nasal, respectively). The PRDS (R_1 , R_2 , R_3 , and R_4) were normalized for each subject by $NR_i = R_i / \sum_{j=1}^4 R_j$. With 10 sets of (NR_1 , NR_2 , NR_3 , and NR_4), we are able to calculate the mean and standard deviation of normalized average PRDS [Fig. 6(a)] in each of the four quadrants. In a similar way, mean and standard deviation of normalized average ADS in each quadrant are also calculated

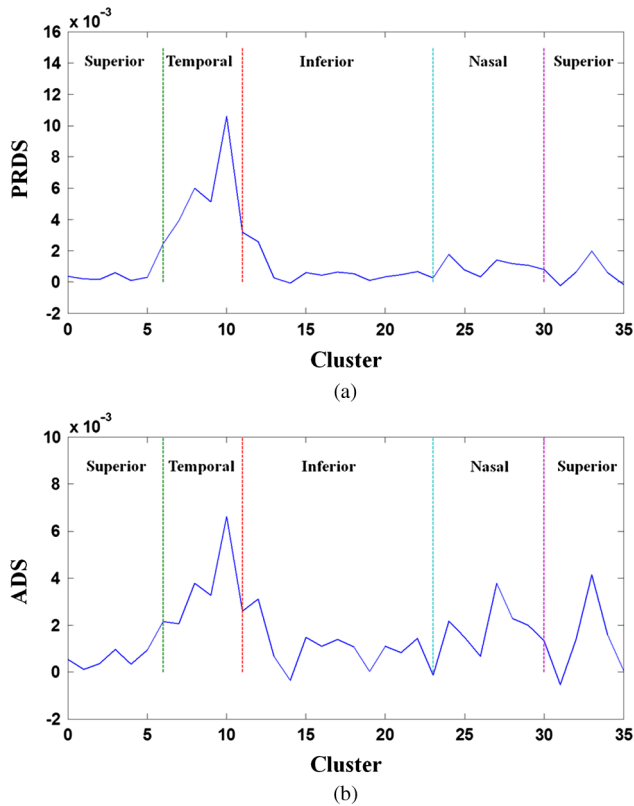


Fig. 5 (a) PRDS versus cluster. (b) ADS versus cluster. Quadrants are separated by dashed lines.

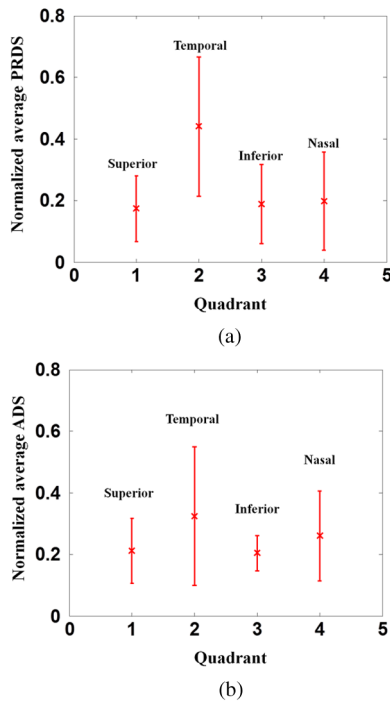


Fig. 6 (a) Mean and standard deviation of 10 subjects' normalized average PRDS in each quadrant. (b) Mean and standard deviation of 10 subjects' normalized average ADS in each quadrant.

Table 1 Paired *t*-test *p*-value (two-tail) of normalized average PRDS for superior versus temporal, inferior versus temporal, and nasal versus temporal quadrants.

	<i>p</i> -value (two-tail)
Superior versus temporal	0.023
Inferior versus temporal	0.021
Nasal versus temporal	0.065

Table 2 Paired *t*-test *p*-value (two-tail) of normalized average ADS for superior versus temporal, inferior versus temporal, and nasal versus temporal quadrants.

	<i>p</i> -value (two-tail)
Superior versus temporal	0.302
Inferior versus temporal	0.127
Nasal versus temporal	0.589

[Fig. 6(b)]. The strongest degradation in DOP with increasing RNFL depth is observed in the temporal quadrant compared with the other three quadrants.

A paired *t*-test (Table 1) is applied to examine the difference in normalized average PRDS between superior and temporal, inferior and temporal, and nasal and temporal. The two-tail *p*-values for superior compared with temporal (0.023) and inferior compared with temporal (0.021) show statistical significance (<0.05).

The paired *t*-test for normalized average ADS is also presented (Table 2). In this case, the difference between temporal quadrant and other three quadrants (superior, inferior, and nasal) does not show statistical significance. According to Eqs. (1) and (2), phase retardation variation relates directly to the DOP, and we consider normalized average PRDS as a better indicator of depolarization and it can be used to distinguish the temporal from the other three quadrants.

4 Discussion and Conclusions

For a PS-OCT system, polarimetric noise includes contributions from instrumentation and the sample tissue. In fiber-based PS-OCT systems, PMD⁴⁰ in fiber and optical components, such as the circulator, are believed to contribute to the polarimetric noise in the birefringence measurement,^{41,42} and approaches have been proposed to compensate for the PMD introduced by SMF and other optical components.⁴³ Structural properties of tissue also contribute to polarimetric noise. When light propagates in tissue, multiple scattering events can randomize the phase retardation, and scattering caused by an irregularly shaped tissue structures can introduce an abrupt change in polarization state of backscattered light. The application of tissue's depolarization property includes segmentation of the depolarization layer by examining DOPU.⁴⁴

Reduction in the DOP with increasing RNFL depth is found to vary between RNFL quadrants. As presented in Fig. 6 and Table 1, superior and inferior quadrants exhibit less reduction

in the DOP, the nasal quadrant has relatively stronger reduction in the DOP, and temporal has the most significant reduction. In RNFL, superior and inferior quadrants have higher microtubule density than temporal and nasal quadrants; superior and inferior quadrants have the highest birefringence. In the temporal quadrant, RGC axons are known to have the smallest diameter⁴⁵ and presumably exhibit a larger scattering angle than the other three quadrants; we expect that a larger scattering angle is associated with increasing impact of scattering events and can introduce higher polarimetric noise and reduce the DOP of incident light. Highest PRDS and ADS are observed in the temporal quadrant. The assumption of a larger scattering angle in the temporal quadrant can be verified by measuring and comparing the backscattering angle of different quadrants. Healthy human subjects' normalized average PRDS and ADS data suggest that phase retardation deviation is a better indicator of depolarization than amplitude deviation and can be used to distinguish the temporal quadrant from the other three quadrants (superior, inferior, and nasal).

In this study, an SMF-based SS PS-OCT system is constructed, and a polarization processing method is developed for investigation of degradation in the DOP with increasing RNFL depth. An increase in phase retardation deviation with increasing RNFL depth is observed and demonstrates degradation in DOP. Ten healthy subjects' cluster ring scan polarization data are analyzed and suggest that the difference in degradation of the DOP between quadrants may be associated with structural properties of microtubules in RNFL axons.

Acknowledgments

The authors gratefully acknowledge support from the National Institutes of Health (NIH R01EY016462).

References

- D. Huang et al., "Optical coherence tomography," *Science* **254**(5035), 1178–1181 (1991).
- A. F. Fercher et al., "Measurement of intraocular distances by backscattering spectral interferometry," *Opt. Commun.* **117**(1–2), 43–48 (1995).
- G. Häusler and M. W. Lindner, "'Coherence radar' and 'spectral radar'—new tools for dermatological diagnosis," *J. Biomed. Opt.* **3**(1), 21–31 (1998).
- S. H. Yun et al., "High-speed wavelength-swept semiconductor laser with a polygon-scanner-based wavelength filter," *Opt. Lett.* **28**(20), 1981–1983 (2003).
- M. A. Choma et al., "Sensitivity advantage of swept source and Fourier domain optical coherence tomography," *Opt. Express* **11**(18), 2183–2189 (2003).
- R. Leitgeb, C. K. Hitzenberger, and A. F. Fercher, "Performance of Fourier domain vs. time domain optical coherence tomography," *Opt. Express* **11**(8), 889–894 (2003).
- J. F. de Boer et al., "Improved signal-to-noise ratio in spectral-domain compared with time-domain optical coherence tomography," *Opt. Lett.* **28**(21), 2067–2069 (2003).
- W. Wieser et al., "Multi-megahertz OCT: high quality 3D imaging at 20 million A-scans and 4.5 GVoxels per second," *Opt. Express* **18**(14), 14685–14704 (2010).
- M. R. Hee et al., "Polarization-sensitive low-coherence reflectometer for birefringence characterization and ranging," *J. Opt. Soc. Am. B* **9**(6), 903–908 (1992).
- J. F. de Boer et al., "Two-dimensional birefringence imaging in biological tissue by polarization-sensitive optical coherence tomography," *Opt. Lett.* **22**(12), 934–936 (1997).
- C. E. Saxer et al., "High-speed fiber based polarization-sensitive optical coherence tomography of in vivo human skin," *Opt. Lett.* **25**(18), 1355–1357 (2000).
- B. H. Park et al., "In vivo burn depth determination by high-speed fiber-based polarization sensitive optical coherence tomography," *J. Biomed. Opt.* **6**(4), 474–479 (2001).
- B. Cense et al., "In vivo depth-resolved birefringence measurements of the human retinal nerve fiber layer by polarization-sensitive optical coherence tomography," *Opt. Lett.* **27**(18), 1610–1612 (2002).
- D. P. Davé, T. Akkin, and T. E. Milner, "Polarization-maintaining fiber-based optical low-coherence reflectometer or characterization and ranging of birefringence," *Opt. Lett.* **28**(19), 1775–1777 (2003).
- E. Götzinger et al., "Polarization maintaining fiber based ultra-high resolution spectral domain polarization sensitive optical coherence tomography," *Opt. Express* **17**(25), 22704–22717 (2009).
- M. K. Al-Qaisi and T. Akkin, "Swept-source polarization-sensitive optical coherence tomography based on polarization-maintaining fiber," *Opt. Express* **18**(4), 3392–3403 (2010).
- B. H. Park et al., "Jones matrix analysis for a polarization-sensitive optical coherence tomography system using fiber-optic components," *Opt. Lett.* **29**(21), 2512–2514 (2004).
- B. H. Park et al., "Optic axis determination accuracy for fiber-based polarization-sensitive optical coherence tomography," *Opt. Lett.* **30**(19), 258–2589 (2005).
- N. J. Kemp et al., "Depth-resolved optic axis orientation in multiple layered anisotropic tissues measured with enhanced polarization-sensitive optical coherence tomography (EPS-OCT)," *Opt. Express* **13**(12), 4507–4518 (2005).
- M. Yamanari et al., "Polarization-sensitive swept-source optical coherence tomography with continuous source polarization modulation," *Opt. Express* **16**(8), 5892–5906 (2008).
- J. Park et al., "Complex polarization ratio to determine polarization properties of anisotropic tissue using polarization-sensitive optical coherence tomography," *Opt. Express* **17**(16), 13402–13417 (2009).
- B. Elmaanaoui et al., "Birefringence measurement of the retinal nerve fiber layer by swept source polarization sensitive optical coherence tomography," *Opt. Express* **19**(11), 10252–10268 (2011).
- B. Baumann et al., "Swept source/Fourier domain polarization sensitive optical coherence tomography with a passive polarization delay unit," *Opt. Express* **20**(9), 10229–10241 (2012).
- T. Torzicky et al., "Retinal polarization-sensitive optical coherence tomography at 1060 nm with 350 kHz A-scan rate using a Fourier domain mode locked laser," *J. Biomed. Opt.* **18**(2), 026008 (2013).
- S. Jiao, G. Yao, and L. V. Wang, "Depth-resolved two-dimensional Stokes vectors of backscattered light and Mueller matrices of biological tissue measured with optical coherence tomography," *Appl. Opt.* **39**(34), 6318–6324 (2000).
- S. Jiao and L. V. Wang, "Jones-matrix imaging of biological tissues with quadruple-channel optical coherence tomography," *J. Biomed. Opt.* **7**(3), 350–358 (2002).
- S. Jiao et al., "Optical-fiber-based Mueller optical coherence tomography," *Opt. Lett.* **28**(14), 1206–1208 (2003).
- X. R. Huang and R. W. Knighton, "Microtubules contribute to the birefringence of the retinal nerve fiber layer," *Invest. Ophthalmol. Visual Sci.* **46**(12), 4588–4593 (2005).
- E. Götzinger et al., "Retinal pigment epithelium segmentation by polarization sensitive optical coherence tomography," *Opt. Express* **16**(21), 16410–16422 (2008).
- J. F. de Boer and T. E. Milner, "Review of polarization sensitive optical coherence tomography and Stokes vector determination," *J. Biomed. Opt.* **7**(3), 359–371 (2002).
- J. Park et al., "Differential geometry of normalized Stokes vector trajectories in anisotropic media," *J. Opt. Soc. Am. A* **23**(3), 679–690 (2006).
- B. Hyle Park et al., "In vivo burn depth determination by high-speed fiber-based polarization sensitive optical coherence tomography," *J. Biomed. Opt.* **6**(4), 474–479 (2001).
- W. L. Bragg and A. B. Pippard, "The form birefringence of macromolecules," *Acta Cryst.* **6**(11–12), 865–867 (1953).
- M. Born and E. Wolf, *Principles of Optics*, 7th expanded ed., Cambridge University Press, Cambridge, England (1999).
- B. Hyle Park et al., "Real-time fiber-based multi-functional spectral-domain optical coherence tomography at 1.3 μm ," *Opt. Express* **13**(11), 3931–3944 (2005).

36. S. Yazdanfar et al., "Frequency estimation precision in Doppler optical coherence tomography using the Cramer-Rao lower bound," *Opt. Express* **13**(2), 410–416 (2005).
37. M. Mujat et al., "Autocalibration of spectral-domain optical coherence tomography spectrometers for in vivo quantitative retinal nerve fiber layer birefringence determination," *J. Biomed. Opt.* **12**(4), 041205 (2007).
38. M. Yamanari et al., "Phase retardation measurement of retinal nerve fiber layer by polarization-sensitive spectral-domain optical coherence tomography and scanning laser polarimetry," *J. Biomed. Opt.* **13**(1), 014013 (2008).
39. E. Götzinger et al., "Retinal nerve fiber layer birefringence evaluated with polarization sensitive spectral domain OCT and scanning laser polarimetry: a comparison," *J. Biophotonics* **1**(2), 129–139 (2008).
40. J. P. Gordon and H. Kogelnik, "PMD fundamentals: polarization mode dispersion in optical fibers," *Proc. Natl. Acad. Sci. U. S. A.* **97**(9), 4541–4550 (2000).
41. E. Z. Zhang and B. J. Vakoc, "Polarimetry noise in fiber-based optical coherence tomography instrumentation," *Opt. Express* **19**(18), 16830–16842 (2011).
42. M. Villiger et al., "Artifacts in polarization-sensitive optical coherence tomography caused by polarization mode dispersion," *Opt. Lett.* **38**(6), 923–925 (2013).
43. E. Z. Zhang et al., "Numerical compensation of system polarization mode dispersion in polarization-sensitive optical coherence tomography," *Opt. Express* **21**(1), 1163–1180 (2013).
44. T. Torzicky et al., "Automated measurement of choroidal thickness in the human eye by polarization sensitive optical coherence tomography," *Opt. Express* **20**(7), 7564–7574 (2012).
45. G. M. Pocock et al., "The relationship between retinal ganglion cell axon constituents and retinal nerve fiber layer birefringence in the primate," *Invest. Ophthalmol. Visual Sci.* **50**(11), 5238–5246 (2009).

Biographies of the authors are not available.